Biomech Model Mechanobiol (2014) 13:463–476
DOI 10.1007/s10237-013-0509-9

ORIGINAL PAPER

Cellular blebs: pressure-driven, axisymmetric, membrane protrusions

Thomas E. Woolley · Eamonn A. Gaffney · James M. Oliver · Ruth E. Baker · Sarah L. Waters · Alain Goriely

Received: 3 April 2013 / Accepted: 18 June 2013 / Published online: 16 July 2013

Abstract Blebs are cellular protrusions that are used by cells for multiple purposes including locomotion. A mechanical model for the problem of pressure-driven blebs based on force and moment balances of an axisymmetric shell model is proposed. The formation of a bleb is initiated by weakening the shell over a small region, and the deformation of the cellular membrane from the cortex is obtained during inflation. However, simply weakening the shell leads to an area increase of more than 4 %, which is physically unrealistic. Thus, the model is extended to include a reconfiguration process that allows large blebs to form with small increases in area. It is observed that both geometric and biomechanical constraints are important in this process. In particular, it is shown that although blebs are driven by a pressure difference across the cellular membrane, it is not the limiting factor in determining bleb size.

Keywords Bleb · Shell model · Force balance · Membrane growth · Cell mechanics

1 Introduction

In this paper, we are interested in using solid mechanics to model the cellular membrane and understand its ability to undergo large deformations (Maugis et al. 2010; Otto et al. 2011; Collins-Hooper et al. 2012; Lew 2003; Schütz and Keller 1998). In particular, we focus on protrusions known as blebs (Charras et al. 2008) (see Fig. 1), which are small spherical blisters in the cellular membrane.

T. E. Woolley (✉) · E. A. Gaffney · J. M. Oliver · R. E. Baker · S. L. Waters · A. Goriely
Mathematical Institute, University of Oxford, 24-29 St Giles, Oxford OX1 3LB, UK
e-mail: woolley@maths.ox.ac.uk

Originally, blebs were thought to be pathological in nature as they had only been observed in apoptotic cells (Robertson et al. 1978; Mills et al. 1998; Russell et al. 1972). More recently, they have been seen to play roles in a number of important cellular phenomena (Paluch et al. 2006; Charras and Paluch 2008), such as cytokinesis (Hickson et al. 2006; Boucrot and Kirchhausen 2007); cell spreading (Norman et al. 2010; Cunningham 1995); and locomotion in tumour, embryonic and stem cells (Otto et al. 2011; Blaser et al. 2006; Sahai and Marshall 2003; Fackler and Grosse 2008; Keller and Eggli 1998; Keller and Bebie 1996).

These protrusions are driven by a pressure difference across the cell membrane and have no apparent internal structure during their initiation. Initially, the membrane is attached to a supporting actin cortex through adhesion proteins. Myosin motors pull on the proteins tensioning the membrane and pressurising the internal cytoplasm. Upon delamination of the membrane from the cortex, cytosol is driven into the weakened region by stress gradients, thereby producing a spherically shaped extension (Charras 2008) (see Fig. 2).

A number of approaches have been used to consider variations of this biological phenomena, although few note the problem of stretching the cellular membrane more than 4 % (Nichol and Hutter 1996; Dai and Sheetz 1999; Sheetz et al. 2006), which is a main concern of our model. Other groups have also used elastic membranes to model bleb formation but have modelled the cortex and cellular membrane separately, allowing consideration of the adhesions (Strychalski and Guy 2012; Young and Mitran 2010; Lim et al. 2012). However, in these cases, the models are restricted to one- or two-dimensional membranes. In the particular case of Young and Mitran (2010), a Newtonian fluid interacts with elastic structures modelling the membrane and filaments.

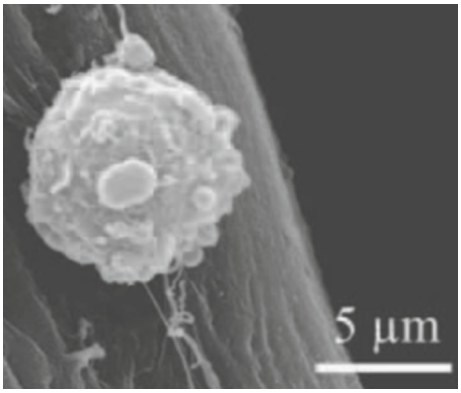

Fig. 1 Scanning electron microscope image of a blebbing cell (Collins-Hooper et al. 2012)

The membrane model depends on a wave equation coupled to various intercellular forces, which leads to blebs with non-spherical-like geometries and non-local interactions.

The model by Tinevez et al. (2009) is based on axisymmetric, non-growing solid mechanics. Through this, they are able to theoretically explain experimental correlations between bleb size and membrane tension. However, they assume linear stress–strain constitutive equations, which only hold under small deformations, and further, they neglect mechanical bending effects.

A full three-dimensional particle-based computational simulation of cellular membrane has been created by Spangler et al. (2011). Here, a triangulated mesh of particles coupled by springs forms the actin cortex, whilst further springs are added to create adhesion bonds between the membrane and the cortex. Not only are they able to produce bleb-like protrusions once the adhesions have been ablated, but they also demonstrate that if the membrane area is bigger than the cortex area on which it is attached, then the bleb morphologies are energetically favourable.

Although single blebs can be nucleated by laser (Tinevez et al. 2009), it is often observed that cells are able to produce multiple blebs that appear over the entire cell. We assume that all blebs are approximately identical, and thus, in this paper, we focus on the formation of a single bleb along the axis of symmetry. The influence that a bleb exerts on another bleb is outside the scope of this model. Critically, the mechanical system we construct depends only on force and moment balances. Further, due to our assumption of axisymmetry, we are able to consider influences that only exist when a three-dimensional structure is considered. The membrane and cortex are idealised as an axisymmetric elastic shell that surrounds pressurised cytosol (Evans 1983). The stress–strain equations in our framework are derived in complete generality, allowing any relation to be postulated. In our case, we consider functional dependencies that arise from large deformation theory in order to capture the considerable change in morphology that occurs when a bleb is formed. Moreover, we include a description of membrane bending and show that it plays an important role in the formation of neck regions that connect the membrane protrusions to the cell body. Assuming constant volume [as suggested by Charras et al. (2008)], the shell is weakened locally to model the delamination of the membrane from the cortex. Although this system is able to produce bleb-like structures in order to do so, we see that the shell has to stretch much more than 4 %. Thus, to make the model more physically accurate, membrane growth is included by allowing the reference configuration to update and reconfigure in order to maintain a strain of $<4\,\%$. How this extra membrane is produced is not suggested; however, it is possible that wrinkles in the membrane are able to unfurl, dramatically increasing the amount of membrane available (Hallett et al. 2008; Hallett and Dewitt 2007), or the membrane can be produced through a combination of endo- and exo-cytosis (Charras et al. 2008).

We begin in Sect. 2 by deriving a system of ODEs that characterise the force balance of the shell. In Sect. 3, we demonstrate the ability of the system to produce solutions over pertinent ranges of parameter values. Further, we compare these results with a purely geometrical model involving two coupled spheres (Hu 2009) (recapitulated in "Appendix"), demonstrating that the two spheres model is only a good comparison to the mechanically dependent problem in certain parameter regimes.

In Sect. 4, we expand upon our basic model with the inclusion of membrane growth. This allows us to maintain a membrane area stretch of $<4\,\%$ whilst producing realistically

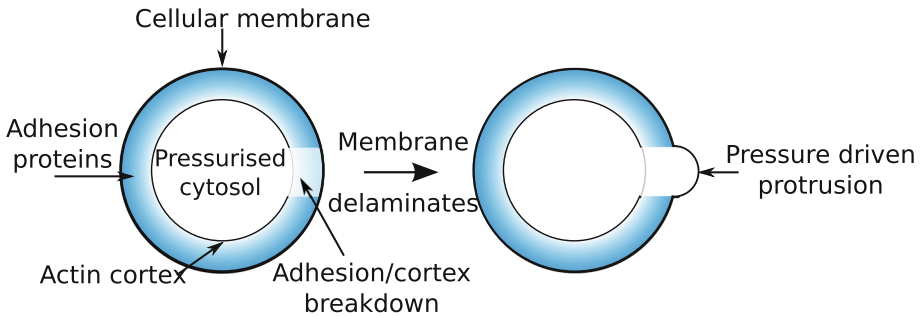

Fig. 2 The main physical process leading to a blebbing cell

sized blebs, thereby increasing the range of validity of our model. In Sect. 5, we compare the growing and non-growing model results. Finally, in Sect. 6, we draw conclusions and highlight experimental results that can be understood within the framework of our model.

2 The mechanical model

We begin by considering an axisymmetric elastic shell (which, by definition, is able to support bending stresses) surrounding a pressurised incompressible fluid. The shell stiffness can be reduced in certain regions of the membrane to model the initiation of bleb-like structures. We do not consider the expansion phase dynamically. Instead, we use the fact that bleb equilibration is very fast (on the order of seconds) to justify the use of an adiabatic approximation, in the sense that, as the weakening occurs, the cell rapidly reaches a static equilibrium. The following derivation of the axisymmetric elastic shell is adopted from those found in (Evans and Skalak 1980; Tongen et al. 2006; Goriely and Tabor 2006, 2003a,b; Goriely et al. 2005) and forms the mechanical basis of the subsequent bleb models.

2.1 Kinematics

The basic geometric set-up is illustrated in Fig. 3. The surface, $\mathcal{S}$, is generated by revolving the curve, $\mathcal{C}$, about the z axis. The curve, $\mathcal{C}$, is parameterised by the material coordinate $0 \leq \sigma \leq L$, which is the arc length in the reference configuration, and thus, $\sigma = 0$ denotes the right-most point at which $\mathcal{C}$ intercepts the z axis.

In addition to the normal Euclidean basis, $\boldsymbol{e}_x$, $\boldsymbol{e}_y$ and $\boldsymbol{e}_z$, we define a right-handed local basis, $\boldsymbol{e}_s$, $\boldsymbol{e}_\phi$ and $\boldsymbol{n}$, on the surface $\mathcal{S}$: $\boldsymbol{e}_s$ is tangent to the curve $\mathcal{C}$ and points in the direction of increasing σ; $\boldsymbol{n}$ is the outward pointing normal to the surface $\mathcal{S}$; and $\boldsymbol{e}_\phi$ is perpendicular to both $\boldsymbol{e}_s$ and $\boldsymbol{n}$ and points in the direction of increasing ϕ.

The exact form of the curve, $\mathcal{C}$, and hence the surface, $\mathcal{S}$, can be described through two variables, y and θ, which depend on σ. Here, $y(\sigma)$ is the distance between the surface and the z axis along the $\boldsymbol{e}_y$ direction and $\theta(\sigma)$ is the angle between the normal of $\mathcal{C}$ at σ, $\boldsymbol{n}(\sigma, \phi)$ and the z axis. The arc length along $\mathcal{C}$, $s(\sigma)$, is measured from the intercept of the curve with the z axis such that $s(0) = 0$. Two further important measures of the geometry of the surface are introduced. These are the principal curvatures, κ_s and κ_ϕ, of a surface (Pressley 2010). In the current axisymmetric form, the curvatures have the explicit form

$$\kappa_s = \frac{\partial \theta}{\partial s} \quad \text{and} \quad \kappa_\phi = \frac{\sin(\theta)}{y}. \tag{1}$$

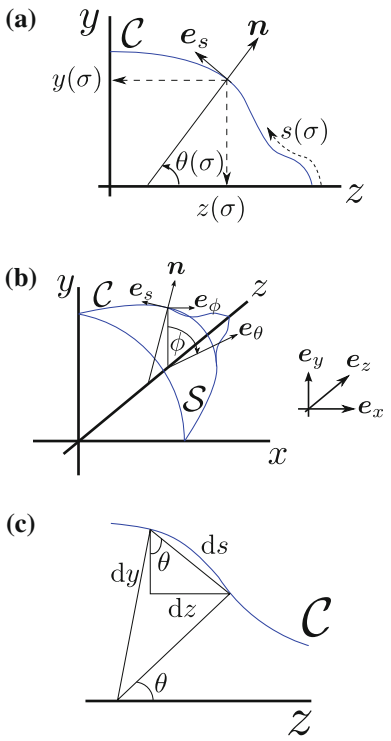

Fig. 3 Geometry of the problem. **a** A $y - z$ plane view of the curve that is to form the surface of revolution. **b** A three-dimensional view of the surface. **c** Linking derivatives to geometric variables

Finally, from Fig. 3c, we see that the derivatives of y and s along $\mathcal{C}$ satisfy

$$\frac{\partial y}{\partial s} = \cos(\theta) \quad \text{and} \quad \frac{\partial z}{\partial s} = -\sin(\theta). \tag{2}$$

Next, we consider a deformation with respect to a reference configuration. The new axisymmetric configuration is completely defined by considering the stretching of the geometric coordinates (see Fig. 4). The *radial stretch ratio*,

$$\lambda_\phi = \frac{y}{y_{\text{rc}}}, \tag{3}$$

is the axisymmetric deformation, where y_{rc} is the vertical coordinate of the reference configuration. The *stretch ratio*,

$$\lambda_s = \frac{\partial s}{\partial \sigma}, \tag{4}$$

measures the local stretching of the body coordinates with respect to arc length.

Finally, we define the unstressed reference configuration of the cell to be a sphere, centred at the origin with radius ρ; thus, $\sigma \in [0, \rho\pi]$ and

$$\lambda_\phi = \frac{y}{\rho \sin(\sigma/\rho)}. \tag{5}$$

Later, in Sect. 4, the reference configuration, and therefore its arc length, will be able to evolve. This means that the

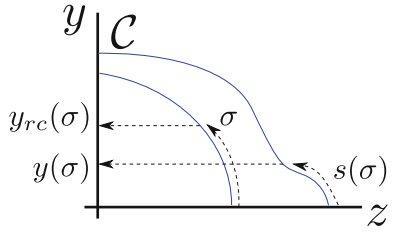

Fig. 4 Linking the reference and solution curves

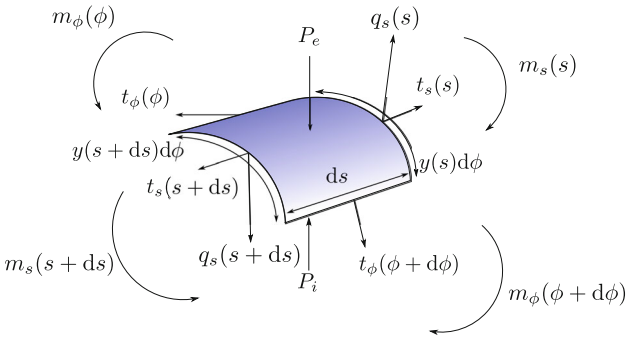

Fig. 5 Small section of the membrane on which the stresses are defined

interval for σ will constantly be updated based on the previous solution.

2.2 Mechanics

We now consider the stresses and moments acting on a small patch of the shell surface of size $\mathrm{d}s$ along $\boldsymbol{e}_s$ and $y\mathrm{d}\phi$ along $\boldsymbol{e}_\phi$, which represents the cellular membrane (see Fig. 5). We assume that the body is in equilibrium and balance forces that are acting in the same direction using geometric links between the curvilinear and Euclidean bases. Here, P_i and P_e are the internal and external pressures acting upon the membrane, respectively. They act normally to the shell surface. The line stresses, t_s and t_ϕ, act along $\boldsymbol{e}_s$ and $\boldsymbol{e}_\phi$, respectively. The normal shear stress, q_s, acts along $\boldsymbol{n}$, and m_s and m_ϕ are the moments about the $\boldsymbol{e}_\phi$ and $\boldsymbol{e}_s$ axes, respectively. Note that these are the only possible non-vanishing moments compatible with axisymmetry. By balancing forces and taking the limit as $\mathrm{d}s$ and $\mathrm{d}\phi$ tend to zero, we obtain

$$(P_i - P_e)\, y\boldsymbol{n} + \frac{\partial\left(yt_s\boldsymbol{e}_s\right)}{\partial s} + \frac{\partial\left(t_\phi\boldsymbol{e}_\phi\right)}{\partial\phi} - \frac{\partial\left(yq_s\boldsymbol{n}\right)}{\partial s} = 0, \quad (6)$$

which can be expanded to give

$$0 = \Delta P y\boldsymbol{n} + \frac{\partial\left(yt_s\right)}{\partial s}\boldsymbol{e}_s - yt_s\kappa_s\boldsymbol{n} - t_\phi y\kappa_\phi\boldsymbol{n} - t_\phi\frac{\partial y}{\partial s}\boldsymbol{e}_s - \frac{\partial\left(yq_s\right)}{\partial s}\boldsymbol{n} - q_s y\frac{\partial\boldsymbol{n}}{\partial s}, \quad (7)$$

where $\Delta P = P_i - P_e$ and $\partial t_\phi/\partial\phi = 0$ by axisymmetry. By resolving in the normal and tangential directions, we obtain

$$\frac{\partial\left(q_s y\right)}{\partial s} = y\left(\Delta P - t_s\kappa_s - t_\phi\kappa_\phi\right), \quad (8)$$

$$\frac{\partial\left(yt_s\right)}{\partial s} = t_\phi\cos(\theta) + q_s y\kappa_s. \quad (9)$$

The moment balance equation is similarly constructed and leads to

$$\frac{\partial\left(m_s y\right)}{\partial s} = m_\phi\cos(\theta) - q_s y. \quad (10)$$

To see that an adiabatic approach is valid, we use the fact that on the observed timescales of bleb expansion, inertial effects are many orders of magnitude less than the dominant terms in the force balance. This can be seen in terms of the following estimation argument. The acceleration component of the force will scale as

$$da\frac{\partial^2 z(0)}{\partial t^2}, \quad (11)$$

where d is the density per unit area of the bleb membrane, a is the blebbed arc length, and $\partial^2 z(0)/\partial t^2$ is the radial acceleration. Using order of magnitude scales such that the cortex-membrane composite shell has a density of water, 10^3 kg/m^3, a width of (less than) 10^{-1} μm, a length scale of 1–2 μm, and a maximum acceleration of the order 1–2 μm/s^2 Eq. (11) has a magnitude of 10^{-15} kg/s^2. This can be compared against the force terms in the right-hand side of equation Eq. (8), which has at least a magnitude of $y\Delta P \sim 10^{-6}$ kg/s^2. This demonstrates that the system perturbations regulating bleb evolution, which are de facto on the timescale of bleb dynamics, are very slow relative to the inertial response timescales.

2.3 Constitutive laws

Using large deformation theory, we relate components of the material strain tensor, e_{ss} and $e_{\phi\phi}$, to the extension ratios (Evans and Skalak 1980):

$$e_{\mathrm{ss}} = \frac{1}{2}\left(\lambda_s^2 - 1\right), \quad (12)$$

$$e_{\phi\phi} = \frac{1}{2}\left(\lambda_\phi^2 - 1\right). \quad (13)$$

These are then linearly related to the surface tensions (Skalak et al. 1973),

$$t_s = Ae_{\mathrm{ss}} + Be_{\phi\phi}, \quad (14)$$

$$t_\phi = Be_{\mathrm{ss}} + Ae_{\phi\phi}, \quad (15)$$

where A and B characterise the elastic properties of the membrane and can vary with σ. Substituting Eqs. (12) and (13) into Eqs. (14) and (15) and remembering $\lambda_\phi = y/\left(\rho\sin(\sigma/\rho)\right)$, it follows that

$$t_s = A\left(\lambda_s^2 + \mu\left(\frac{y}{\rho\sin(\sigma/\rho)}\right)^2 - (1+\mu)\right), \tag{16}$$

$$t_\phi = A\left(\mu\lambda_s^2 + \left(\frac{y}{\rho\sin(\sigma/\rho)}\right)^2 - (1+\mu)\right), \tag{17}$$

where $\mu = B/A$ is a measure of relative extensibility of the membrane in the azimuthal and longitudinal directions. Note that although we use large deformation theory throughout this work, this constitutive framework is only needed in the mechanical case when the reference configuration is not remodelled, as in this situation, large strains occur. In the later case when the reference configuration is updated to maintain an area increase of $<4\,\%$ a linear constitutive relationship would be an appropriate approximation.

Finally, we need to specify constitutive relationships for the bending moments. Here, the bending moments are assumed to be isotropic and proportional to the mean surface curvature, i.e.,

$$m_\phi = m_s = M(\kappa_s + \kappa_\phi - K_0), \tag{18}$$

where K_0 is the initial mean curvature, and M is the bending modulus.

2.4 The ODE system

Collecting all of these equations together and using Eq. (4) to convert from the variable s to σ, we arrive at the following system of seven ODEs:

$$\frac{\partial y}{\partial\sigma} = \lambda_s\cos(\theta), \tag{19}$$

$$\frac{\partial\theta}{\partial\sigma} = \lambda_s\kappa_s, \tag{20}$$

$$\frac{\partial z}{\partial\sigma} = -\lambda_s\sin(\theta), \tag{21}$$

$$\frac{\partial s}{\partial\sigma} = \lambda_s, \tag{22}$$

$$\frac{\partial t_s}{\partial\sigma} = \lambda_s\left(\frac{\cos(\theta)}{y}\left(t_\phi - t_s\right) + \kappa_s q_s\right), \tag{23}$$

$$\frac{\partial q_s}{\partial\sigma} = \lambda_s\left(\Delta P - \kappa_\phi t_\phi - \kappa_s t_s - q_s\frac{\cos(\theta)}{y}\right), \tag{24}$$

$$\frac{\partial\kappa_s}{\partial\sigma} = \lambda_s\left(\frac{\cos(\theta)}{y}\left(\kappa_\phi - \kappa_s\right) - \frac{q_s}{M}\right). \tag{25}$$

For clarity, we repeat that the first four Eqs. (19)–(22) are derived from the geometry of the shell, Eqs. (23) and (24) stem from the force balance, and Eq. (25) arises from the moment balance. Together with Eqs. (16) and (17), Eqs. (19)–(25) constitute a closed system of equations that can be solved on the interval $\sigma \in [0, \rho\pi]$, once appropriate boundary conditions have been prescribed.

Protrusions are generated in the model by weakening the membrane within a small region near $\sigma = 0$. This mimics the biological phenomenon of the membrane delaminating from the cortex. To account for this, we give the parameter A a tanh profile of the form

$$A(\sigma) = A_+\left(1 + \frac{1}{2}\left(1 - \frac{A_-}{A_+}\right) \times \left(\tanh\left((\sigma - \hat{\sigma})\beta\right) - 1\right)\right). \tag{26}$$

Explicitly, A_+ and A_- determine the stiffness of the shell away from, and close to, the bleb region, respectively, $\hat{\sigma}$ controls the amount of membrane that is weakened, and finally, β defines the length scale over which delamination occurs. Due to the adhesion acting over a very small length scale, we expect the transition between the stiff and softer sections of the cell to be very quick, and thus, throughout all the simulations, we use $\beta = 20\,\mu\mathrm{m}^{-1}$.

Before we prescribe boundary conditions, we notice that this system of ODEs admits a first integral. Indeed, fixing ΔP to be constant and using Eqs. (19), (20), (23) and (24), we are able to eliminate t_ϕ and κ_s to produce the constraint

$$0 = \frac{\partial}{\partial s}\left(\Delta P\frac{y^2}{2} - \kappa_\phi y^2 t_s - q_s y\frac{\partial y}{\partial s}\right). \tag{27}$$

This equation encapsulates the result that the balance of forces in the $\boldsymbol{e}_z$ direction is the same everywhere on the shell. Noting that since the cell cuts the z axis at the front (and back) of the cell, then $y = 0$ at $s(0)$ (and $s(\rho\pi)$), and so, by continuity,

$$\frac{\Delta P y}{2} = q_s\cos(\theta) + \kappa_\phi y t_s. \tag{28}$$

Observe that, in the case when bending is not supported, i.e., $q_s = 0$, Eq. (28) reduces to Laplace's law for an axisymmetric membrane.

Equations (16) and (28) allow us to eliminate t_s completely, thus reducing the number of dependent variables from seven to six. This number can further be reduced by noticing that Eqs. (21) and (22) decouple from the system, leaving only four equations in $(y, \theta, q_s, \kappa_s)$, which need to be solved as a boundary value problem (BVP). The remaining two equations constitute an initial value problem once the BVP is solved.

2.5 Boundary conditions

Having reduced the number of equations in the system, we set $y = 0$ at $\sigma = 0$ and $\pi\rho$ and $\theta = 0$ and π at $\sigma = 0$ and $\pi\rho$. Thus, we have four boundary conditions and four unknown variables, producing a correctly posed problem. However, the geometric singularities at $\sigma = 0$ and $\pi\rho$ cause numerical integrators to have difficulty when converging near these points. In order to maintain control over the regularity of the solution at these points, we perturb the solution interval away from the singularities and use Eqs. (19)–(25) to produce

consistency equations that need to be satisfied at each end of the shell.

We consider a solution interval to be $\sigma \in [\epsilon, \pi\rho - \epsilon]$. We then Taylor expand the ODE system close to $\sigma = 0$ and $\sigma = \pi\rho$ using expansions of the form

$$y^0 = y_0^0 + \sigma y_1^0 + \sigma^2 y_2^0 + \ldots, \tag{29}$$

and

$$y^\infty = y_0^\infty + (\pi\rho - \sigma) y_1^\infty + (\pi\rho - \sigma)^2 y_2^\infty + \ldots, \tag{30}$$

respectively. The other variables, θ, q_s and k_s, have similar perturbation expansions. To first order, we satisfy the desired boundary conditions as stated above; thus, $y_0^0 = y_0^\infty = 0 = \theta_0^0$ and $\theta_0^\infty = \pi$. By considering Eq. (28), we also note that to first order, q_s is zero at the boundaries.

Upon substitution of these expansions into the ODE system, we find that there is a term of order $O(\epsilon^{-1})$ in Eq. (25). To eliminate this singularity, we must enforce the condition $\theta_1^0 = \kappa_{s0}^0 y_1^0$. Similarly, when $\sigma = \pi\rho - \epsilon$, we find that $\theta_1^\infty = \kappa_{s0}^\infty y_1^\infty$. At order $O(\epsilon^0)$, we find $y_1^0 = \lambda_{s0}^0$. Using Eqs. (16) and (28), we can derive the form of λ_{s0}^0, from which we find that y_1^0 is given implicitly by the following cubic:

$$\kappa_{s0}^0(1+\mu)\left(y_1^0\right)^3 - \left(\frac{\Delta P}{2} + \kappa_{s0}^0 A(0)(1+\mu)\right) y_1^0 + q_{s1}^0 = 0. \tag{31}$$

By construction, we take the root, y_1^0, that connects continuously to the real, positive root that exists when $q_{s1}^0 = 0$. The condition at the opposite edge is similar except that the sign of the q_{s1}^0 term is now negative, and we evaluate the stiffness parameter, A, at $\sigma = \pi\rho$. In summary, the prescribed boundary conditions are

$$\begin{aligned} y(\epsilon) &= y_1^0 \epsilon, \\ \theta(\epsilon) &= \kappa_{s0}^0 y_1^0 \epsilon, \\ y(\pi\rho - \epsilon) &= y_1^\infty \epsilon, \\ \theta(\pi\rho - \epsilon) &= \pi - \kappa_{s0}^\infty y_1^\infty \epsilon, \end{aligned}$$

where y_1^0, y_1^∞, κ_{s0}^0, κ_{s0}^∞, q_{s1}^0 and q_{s1}^∞ are found implicitly as part of the BVP, using Eq. (31) and its analogue derived at $\sigma = \pi\rho - \epsilon$.

3 Results of mechanical model

We first consider the mechanical response of a cell membrane undergoing localised weakening. This weakening occurs by letting the stiffness parameter, A, in Eqs. (16) and (17) that vary according to Eq. (26). We use the pressure difference, ΔP, as a Lagrange multiplier in order to keep the cell volume constant (Charras et al. 2008). Thus, as a protrusion develops and grows, the rest of the cell body contracts to compensate and the pressure difference drops.

As for the other parameters, we vary them over physically realistic values as suggested in the literature (Dai and Sheetz 1999; Pozrikidis 2001; Collins-Hooper et al. 2012; Keller and Eggli 1998). In particular, we frequently use an initial pressure difference of 10 Pa, a bending stiffness of $M = 10^{-2}$ pNμm, $\mu = 0.5$ and a cell reference configuration radius of $\rho = 5\,\mu$m. From these values and formula (53) derived in "Appendix," we infer that $A_+ = 10^3$ pN/μm. The Young's modulus, E, can be approximately related to the stiffness parameter A through the relation $A \approx Eh$, where h is the width of the shell. Using $h = 0.1\,\mu$m as an order of magnitude size of the shell, then we see that $E = 10^4$ Pa, which is consistent with biological material properties (Ashby et al. 1995). One of the primary simulated results of interest is the cell profile, and so, in a number of figures, extension of the bleb is used as a measure of cell deformation. The extension is important when considering bleb-based motility, as it has been shown that such motion is greatly retarded if blebs are too small or too big (Otto et al. 2011). Bleb extension is calculated by subtracting the diameter of the unweakened cell from the total width of the weakened cell, which is the distance along the z axis separating the points at $\sigma = \epsilon$ and $\sigma = \rho\pi - \epsilon$.

In Figs. 6 and 7, we see the effects of gradually decreasing the stiffness near $\sigma = 0$. The majority of the shell is fixed with a value of $A_+ = 10^3$ pN/μm, and thus, for a large range of values for A_-, there is no significant change in bleb volume or pressure difference. As noted in the figure, the stiffness must be dropped until it is of the order 1 pN/μm before sizeable blebs are observed. As the stiffness is decreased further, the cell profile begins to change considerably, eventually leading to the extension of a neck region linking two approximately spherical shapes, as reported in the literature (Charras 2008; Charras et al. 2008; Tinevez et al. 2009; Fackler and Grosse 2008). Further, we note that during the formation of these blebs, there is very little change in the radius of the cell body.

Notably, altering certain parameters in the simulations is seen to have a very little effect on the cell's morphology (Fig. 7a). In particular, decreasing the bending stiffness, M, of the shell by five orders of magnitude has little influence on the final bleb volume. This provides an a posteriori illustration that the bending stiffness of the cell is too small to have any discernible effect on bleb volume and can potentially be ignored in later models. Similarly, although alterations in the isotropy parameter, μ, have a large effect on the relationship between volume and shell stiffness, it has qualitatively negligible effects on pressure difference (see Fig. 7b).

We continue to look at the effect of dropping the shell stiffness in Fig. 7b, where we record the response of the pressure difference. As discussed, the pressure difference is used as a

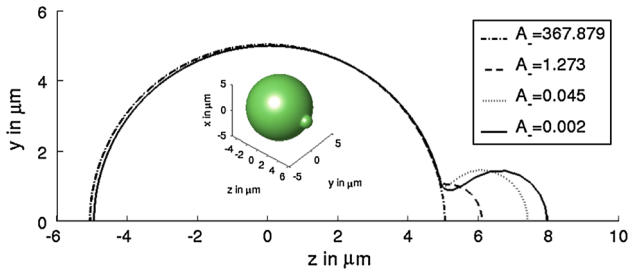

Fig. 6 As the membrane is weakened, the bleb becomes more pronounced. Parameters are either shown in the figure or $A_+ = 10^3$ pN/µm, $\hat{\sigma} = 1\,\mu = 0.5$, $M = 10^{-2}$ pNµm, the initial pressure difference was $\Delta P = 10$ Pa, and the values of A_- are given in the figure and have units pN/µm. The *inset* of the figure shows the surface of revolution generated when $A_- = 1.273$ pN/µm

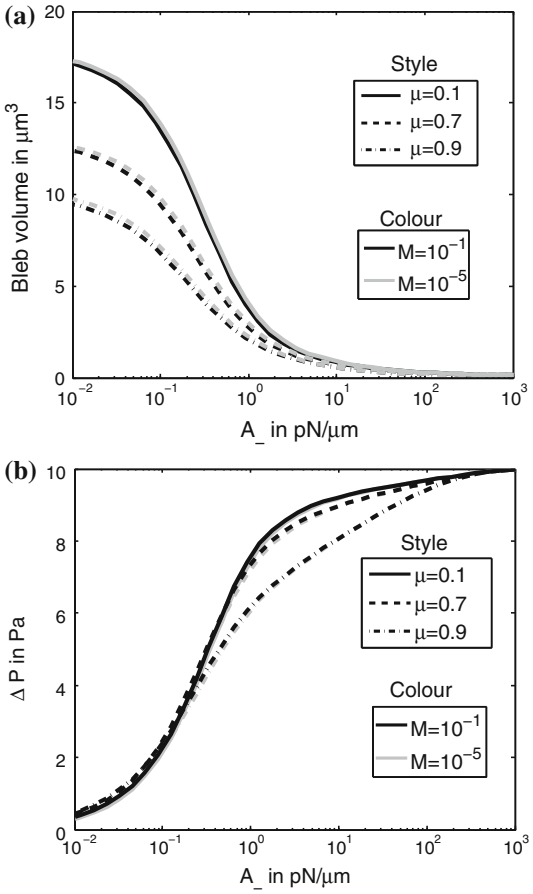

Fig. 7 As the membrane is weakened, the bleb volume becomes larger causing the pressure difference to decrease, in order to maintain a constant volume. Note that the $M = 10^{-1}$ and 10^{-5} pNµm curves are nearly on the top of one another. Parameters are either shown in the figure or $A_+ = 10^3$ pN/µm, $\hat{\sigma} = 1\,\mu = 0.5$, $M = 10^{-2}$ pNµm, and the initial pressure difference was $\Delta P = 10$ Pa

Lagrange multiplier to enforce volume conservation. Clearly, we can see that blebs are able to reduce the pressure difference across the membrane, a property that has been noted in physical cells and used as an experimental tool (Tinevez et al. 2009; Dai and Sheetz 1999).

In Fig. 8, a purely geometric model (derived in "Appendix") (Hu 2009) is compared with simulations of the model derived in this work. Although in Fig. 7b, it was noted that altering the values of M and μ had little effect on the relationship between the pressure difference and the elastic properties of the membrane; here, we observe that, in extreme parameter regimes, they are able to influence the bleb profiles. Figure 8a demonstrates this possibility: towards the upper end of the physically allowable values of μ, the extension for a given bleb volume is underestimated by the geometric model for large values of M, whereas the opposite is observed when M is reduced (Fig. 8b). These effects are confirmed in Fig. 8c, d, where we see that a neck region is able to form because of the larger bending modulus.

Further, for larger values of μ, the pressure has to overcome line tensions in the azimuthal and longitudinal directions. This means blebs of comparable volume are obtained for smaller values of A_-. This reduced stiffness means that the bleb can extend further, as illustrated in Fig. 8a, c. This corroborates what was seen in Fig. 7a, which demonstrates that μ has a significant effect on the relationship between the bleb volume and A_-.

Finally, although Fig. 9a demonstrates the unsurprising relationship that, as the initial internal pressure decreases so does the maximal bleb extension, Fig. 9b illustrates the unforeseen non-monotonic relationship between bleb extension and the arc length of the weakened region. This demonstrates that blebs of the same extension can be obtained with both small and large neck apertures. It also suggests that the amount of membrane that delaminates from the cortex must be carefully controlled by the cell to optimise bleb size.

4 Growth and reconfiguration

When the shell is weakened to $A_- = 368$ pN/µm, the maximal area stretch is 3.88 %. Clearly, this is not enough to produce observed bleb sizes (see Fig. 6), which are closer to the morphology of the shell weakened to $A_- = 1.27$ pN/µm. However, the maximum area stretch in this case takes an unrealistic value of 228 %. This demonstrates why reconfiguration and growth of the cellular membrane must occur.

Due to the fast timescale of bleb formation mentioned in Sect. 2, we explicitly assume that the membrane relaxes on a much faster timescale than the growth of the membrane. Membrane growth is incorporated into the system by evolving the reference configuration. Concordantly, the solution domain is also updated, as it is the arc length of the reference configuration.

By reconfiguring in this way, protrusions naturally emerge even for small strains. System (19)–(25) generates an

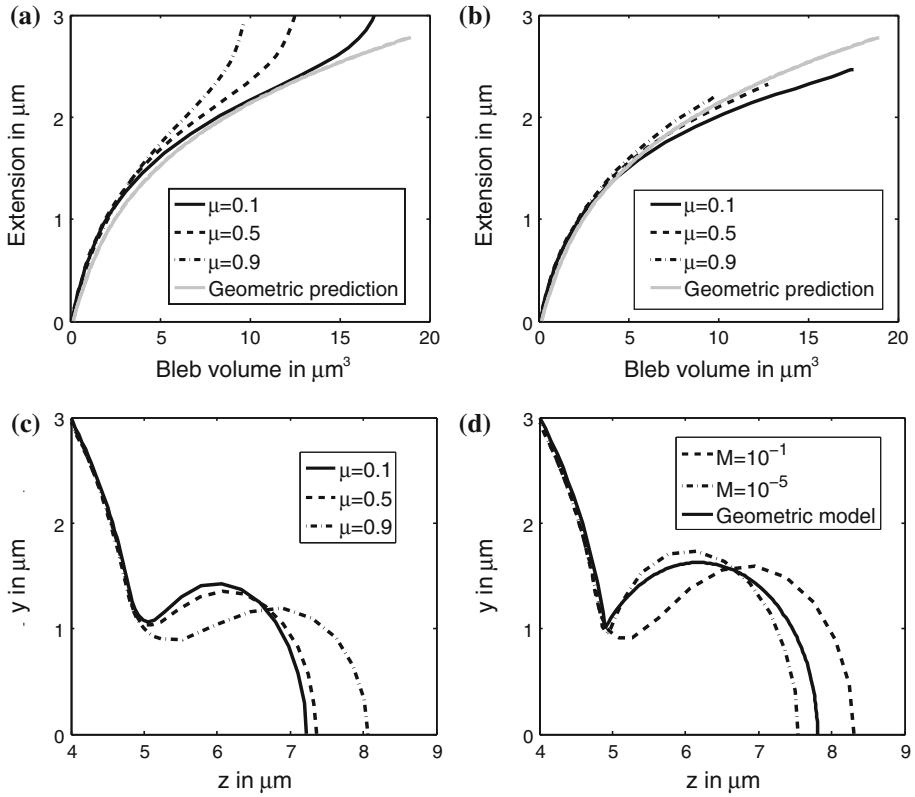

Fig. 8 Correlation between membrane extension and bleb volume compared between simulations of system (19)–(25) and geometric predictions (see "Appendix"). Parameters: **a** $M = 10^{-1}$ pNμm and **b** $M = 10^{-5}$ pNμm. All others parameters are the same in (**a**) and (**b**); $A_+ = 10^3$ pN/μm, $\hat{\sigma} = 1$, and μ is given in the figures. In each case, A_- was reduced from 10^3 to 0.0061 pN/μm. **c** Comparison between the simulated profiles for different values of μ. The parameters were chosen such that each profile has a 9.7 μm^3 bleb volume; $A_+ = 10^3$ pN/μm, $\hat{\sigma} = 1$, and $M = 10^{-1}$ pNμm. For the $\mu = 0.1$ profile, $A_- = 0.24$ pN/μm; for the $\mu = 0.5$ profile, $A_- = 0.088$ pN/μm; and for the $\mu = 0.9$ profile, $A_- = 0.044$ pN/μm. **d** Comparison of the simulated and predicted profiles for different values of M. The parameters were chosen such that each profile has a 17 μm^3 bleb volume; $A_+ = 10^3$ pN/μm, $\hat{\sigma} = 1$, and $\mu = 0.1$. For the $M = 10^{-1}$ pNμm profile, $A_- = 0.006$ pN/μm; and for the $M = 10^{-5}$ pNμm profile, $A_- = 0.009$ pN/μm

equilibrium state only for the given reference configuration. Thus, once the reference configuration is updated, we must resolve the system to find the new equilibrium state, thereby creating an evolution from one equilibrium state to the next.

To close the system, we need to specify an evolution law for the reference configuration. Since strains are small, we assume that the reference configuration relaxes linearly to the current membrane profile. Explicitly, if $y_{\rm rc}(\Sigma, t)$ and $\Sigma = \Sigma(\sigma, t)$ are the profile of the reference configuration and corresponding arc length at time t, respectively, then

$$\left.\frac{\partial y_{\rm rc}}{\partial t}\right|_{\Sigma}(\Sigma, t) = \eta\left(y(\Sigma, t) - y_{\rm rc}(\Sigma, t)\right), \quad y_{\rm rc}(\Sigma, 0) = \rho \sin(\sigma/\rho), \tag{32}$$

and

$$\frac{\partial \Sigma}{\partial t} = \eta\left(s - \Sigma\right), \quad \Sigma(\sigma, 0) = \sigma \in [\epsilon, \hat{\sigma}]. \tag{33}$$

Critically, note that reconfiguration only occurs in the blebbing region $\sigma \in [\epsilon, \hat{\sigma}]$, where $\hat{\sigma}$ denotes the maximum arc length of reference configuration that is weakened (Dai and Sheetz 1999). The boundary conditions can be derived as in Sect. 2.5, and although they stay essentially the same, the expansion Eq. (31) gains an extra factor due to the reference configuration no longer being of the definite form $\rho \sin(\sigma/\rho)$. Namely, if the reference configuration expansion has the form $y_{\rm rc}(\Sigma, t) = \Sigma y^0_{rc1} + \Sigma^2 y^0_{rc2} + \ldots$ as $\Sigma \to 0$, then the boundary condition at $\Sigma = \epsilon$ implies

$$\kappa^0_{s0} A(0) \frac{\left(1 + \mu \left(y^0_{rc1}\right)^2\right)}{\left(y^0_{rc1}\right)^2} \left(y^0_1\right)^3 - \left(\frac{\Delta P}{2} + \kappa^0_{s0} A(0)(1 + \mu)\right) y^0_1 + q^0_{s1} = 0. \tag{34}$$

Since we step through adiabatic iterations, we do not have an explicit representation of continuous time, and so, Eqs. (32) and (33) are applied using discretised forms of the

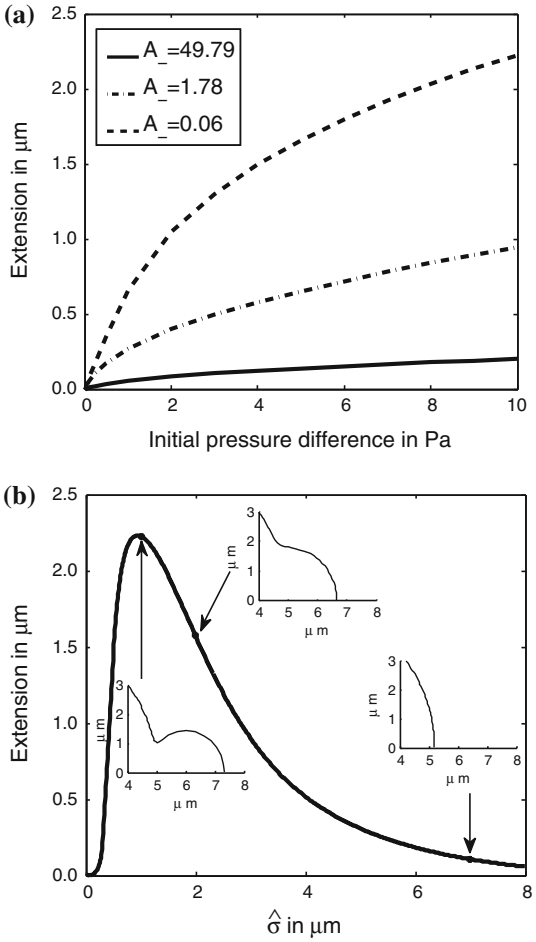

Fig. 9 The change in membrane extension relative to initial pressure is monotonic, but non-monotonic with respect to neck size. Parameters are $A_+ = 10^3$ pN/μm, $A_- = 0.0634$ pN/μm, $\mu = 0.5$, and $M = 10^{-2}$ pNμm. Where not otherwise stated, $\Delta P = 10$ Pa and $\hat{\sigma} = 1$ μm

ODEs, assuming that each iteration takes a time Δt. Explicitly, for the reference configuration, this is

$$y_{\mathrm{rc}}(i+1) = y_{\mathrm{rc}}(i) + \eta \Delta t \left(y(i) - y_{\mathrm{rc}}(i)\right), \tag{35}$$

where $y(i)$ and $y_{\mathrm{rc}}(i)$ are the ith solution and reference configurations, respectively. The discretised equation for the arc length is given *mutatis mutandis*. Although a priori we have no guarantee that Δt will be small enough to allow us to approximate the linear update rule in this manner, we will see in Sect. 5 that Δt is of the magnitude 10^{-2} s, justifying the use of Eq. (35) for our problem.

Through the addition of reconfiguring, not only are we able to reproduce realistic sized blebs with realistic strains, we also gain a timescale that needs to be compared with experiments. Thus, once we have simulated bleb formation, we can use the timescale, $\eta \Delta t$, along with the experimental bleb formation time scale of 30 s, in order to derive a velocity profile of the bleb.

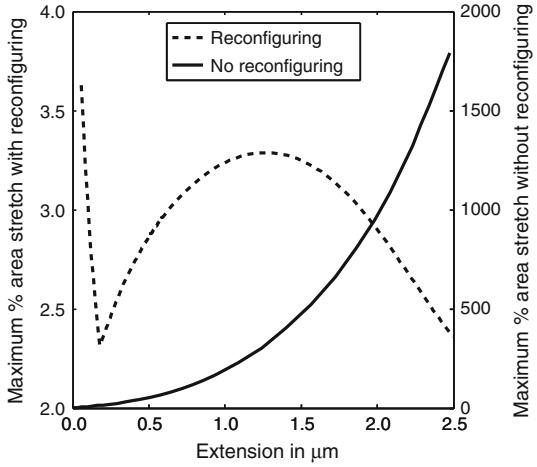

Fig. 10 Comparing the maximum area stretch in the reconfiguring and non-reconfiguring cases. Parameters are $A_+ = 10^3$ pN/μm, $\hat{\sigma} = 1$μm, $\mu = 0.5$, $M = 10^{-2}$ pNμm, and the initial pressure difference was 10 Pa. In the non-reconfiguring case, A_- is reduced from 10^3 to 6×10^{-4} pN/μm, whereas in the reconfiguring case, A_- is reduced to 367.9 pN/μm, with the reference configuration continuously being updated with a timescale of $\eta \Delta t = 0.3$

5 Results with reconfiguration

We consider again the set-up of Sect. 3, but with the inclusion of shell reconfiguration. Equation (26) is used to reduce the stiffness of the front of the shell. However, A_- is only reduced until the increase in local shell area is a maximum of 4 % relative to the reference state. The increase in area is calculated through the product of the azimuthal and arc length stretches, $\lambda_s \lambda_\phi$.

We first compute the maximum of $\lambda_s \lambda_\phi$ as a function of the extension (Fig. 10). We see that before the shell's reference state is reconfigured, the area stretch in the system increases exponentially, far beyond the experimentally estimated values. However, with the inclusion of reconfiguring, large extensions are obtained whilst maintaining an increase in shell area of <4 %, relative to the evolving reference state. Critically, we observe that the area stretch does not undergo a constant or monotonic evolution as the extension increases. Initially, as the membrane reconfigures, the area stretch falls very quickly as the reference configuration evolves closer to the solution configuration. The increase in stretch then occurs as the neck region starts to form. Thus, although λ_ϕ continues to decrease, λ_s increases because the membrane starts to depart from the reference configuration that is not updated, outside of the blebbing region. Physically, this corresponds to the membrane beginning to peel away from the cortex, as observed experimentally (Charras et al. 2008). As the pressure difference drops and the neck region stabilises, the cell body contraction brings the neck region closer to the reference configuration, thereby causing a second reduction in area stretch.

Second, we look at the effect of the update factor $\eta\Delta t$. In Fig. 11a, b we see that as the bleb grows, its growth rate reduces. This is due to the fact that as the bleb grows, the pressure difference, ΔP, decreases in order to conserve the volume (see Fig. 11c). Also observe that, although larger update factors increase the rate at which the cell evolves, this does not affect the relationship between the pressure difference and the bleb extension, which effectively form the same curve. Thus, as we would expect, decreasing the update factor simply increases the number of iterations that it takes to evolve to the same state.

Further, from Fig. 11c, we notice the first quantitative difference between reconfiguring and non-reconfiguring simulations. Although there is very little difference between the pressures for extensions $<1.5\,\mu$m, beyond $1.5\,\mu$m, the two curves start to diverge with the pressure in the non-reconfiguring case dropping more rapidly than the reconfiguring case. Altogether, Fig. 11 suggests that, in the reconfiguration simulations, although the rate of bleb formation decreases because the pressure difference drops, pressure is not the limiting factor for protrusion extension as it might be in the non-reconfiguration simulations. This means that given the same initial pressure difference, the reconfiguration simulations could be iterated further to produce bigger blebs than their non-reconfiguring counterparts.

We continue looking for differences between the reconfiguring and non-reconfiguring cases by considering the change in surface tension over the bleb and cell body as the extension increases. Immediately, we can visually detect the approximately linear relationship (28) between ΔP and t_s as the surface tension curves for the cell body in Fig. 12 match the pressure difference curves in Fig. 11c, up to a scaling factor. Due to this relationship between ΔP and t_s, we should be little surprised that the values of bleb surface tension in the reconfiguring and non-reconfiguring cases are also very close for extensions $<1.5\,\mu$m whilst diverging for larger extensions.

We now consider the velocity profile and its dependence on the update timescale, $\eta\Delta t$. Using a timescale of approximately $T = 30\,$s [as often been reported in the blebbing literature Charras et al. (2008), Charras (2008), Collins-Hooper et al. (2012), Maugis et al. (2010)], we fix the number of reconfiguration iterations, N, at which we define to be a typical bleb size. When $\eta\Delta t = 0.3$, we take $N = 10^3$, as this produces a bleb of radius $1.2\,\mu$m (see Fig. 13), which is the correct order of magnitude. We now substitute these parameters into the equation

$$N\Delta t = T, \tag{36}$$

giving $\Delta t = 3 \times 10^{-2}\,$s, whence $\eta = 10/$s. Assuming η stays constant as $\eta\Delta t$ is reduced, we generate estimates for the number of simulations needed for slower updates. For example, when $\eta\Delta t = 0.2$, we would need

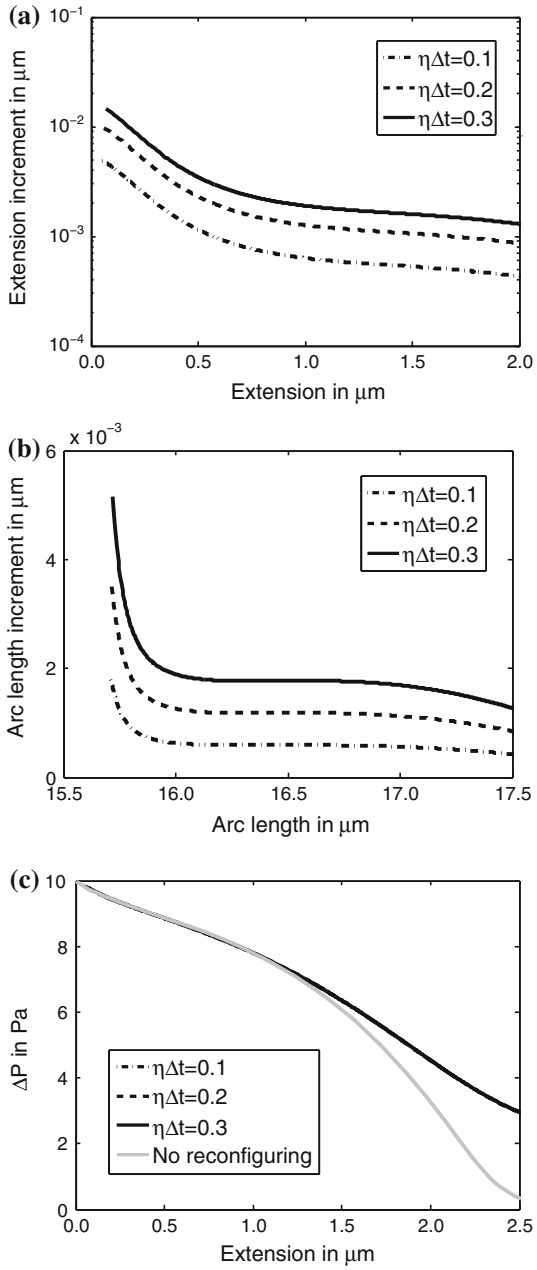

Fig. 11 As the bleb grows through the reconfiguration process, **a** the extension rate, **b** the rate of arc length increase and **c** the pressure difference all decrease. The curves for different $\eta\Delta t$ all lie on the top of each other in (**c**). Parameters are $A_+ = 10^3\,$pN/μm, $A_- = 367.9\,$pN/μm, $\hat{\sigma} = 1$, $\mu = 0.5$, $M = 10^{-2}\,$pNμm, and the initial pressure difference was $\Delta P = 10\,$Pa

$$N = \frac{30}{(0.2/10)} = 1{,}500 \text{ iterations} \tag{37}$$

to produce an equivalent bleb. This excellent correspondence can be seen in Fig. 13.

Further, for each iteration, i, we can calculate $z_0(i)$, the maximal z position at the front of the cell. From Fig. 11a,

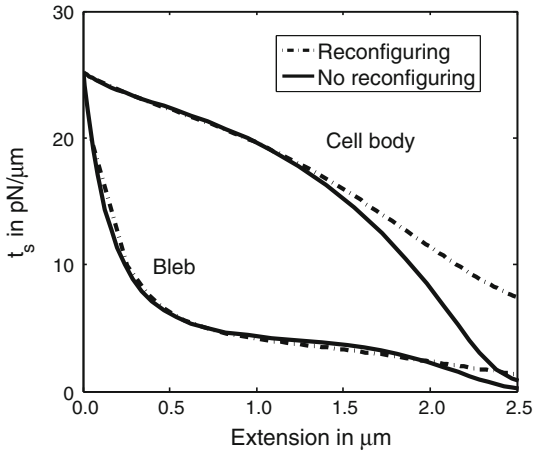

Fig. 12 Maximum surface tension in the bleb and cell body reduces as the bleb grows. Parameters are $A_+ = 10^3\,\text{pN}/\mu\text{m}$, $A_- = 367.9\,\text{pN}/\mu\text{m}$, $\hat{\sigma} = 1$, $\mu = 0.5$, $M = 10^{-2}\,\text{pN}\mu\text{m}$, and the initial pressure difference was $\Delta P = 10\,\text{Pa}$

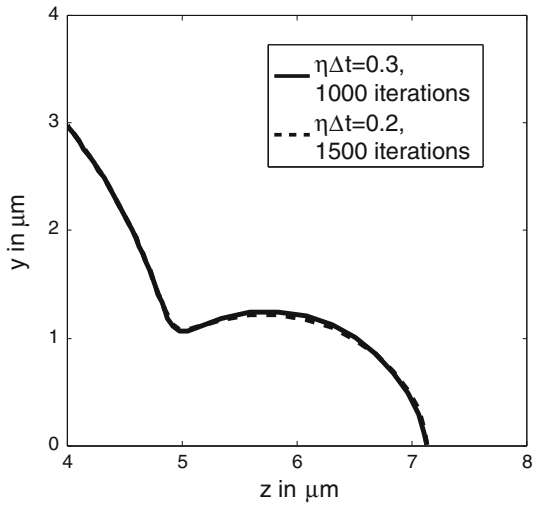

Fig. 13 The number of iterations and the relaxation time scale are related. Parameters are $A_+ = 10^3\,\text{pN}/\mu\text{m}$, $A_- = 367.9\,\text{pN}/\mu\text{m}$, $\hat{\sigma} = 1$, $\mu = 0.5$, $M = 10^{-2}\,\text{pN}\mu\text{m}$, and the initial pressure difference was $\Delta P = 10\,\text{Pa}$

we see that each increment in $z_0(i)$ is small, and thus, we approximate the front velocity, $\partial z(0,t)/\partial t$, by

$$\frac{\partial z(0,t)}{\partial t} \approx \frac{\Delta z_0(i)}{\Delta t} = \frac{z_0(i+1) - z_0(i)}{\Delta t}. \tag{38}$$

Front velocity and corresponding extension are given in Fig. 14. As expected, the protrusion initially extends very quickly, although this rapid expansion period is very brief. This is consistent with experimental data showing similar rapid, but brief expansion, followed by a slower increase in size (Maugis et al. 2010).

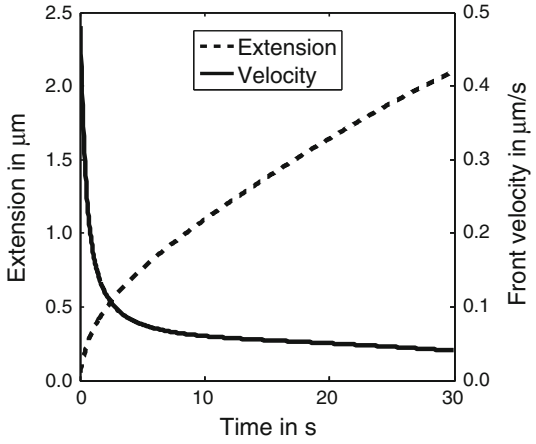

Fig. 14 Speed and extension of the blebbing front. Parameters are $A_+ = 10^3\,\text{pN}/\mu\text{m}$, $A_- = 367.9\,\text{pN}/\mu\text{m}$, $\hat{\sigma} = 1$, $\mu = 0.5$, $M = 10^{-2}\,\text{pN}\mu\text{m}$, $\eta\Delta t = 0.3$, and the initial pressure difference was $\Delta P = 10\,\text{Pa}$

6 Conclusion

Blebs are cellular protrusions that are used by cells for multiple purposes including locomotion. The aim of this paper was to capture some of the mechanical features of the cellular membrane separating from the cortex during the initiation of blebbing. We modelled the cell as an axisymmetric shell. Bleb-like protrusions were created by weakening the shell over a small region near the axisymmetric tip. A purely mechanical model requires that the strains are unrealistically large for observed extensions, and so, we generalised our method to include membrane growth.

Without membrane reconfiguration, the quantitative nature of the results may be of limited value when considering cellular membrane, as the membrane is only able to support a 4 % increase in area before lysis occurs (Nichol and Hutter 1996; Dai and Sheetz 1999; Sheetz et al. 2006). In contrast, the protrusions of observable size, illustrated in Fig. 6, increase the area by 100–1,000 %. A solution illustrating approximately 4 % stretch is shown in Fig. 6 demonstrating that if this is the maximum viable stretch, then more membrane must be generated for sizeable protrusions to be realised. Physically, it is currently a matter of debate as to whether this extra membrane exists naturally in invaginations of the cell (Hallett et al. 2008; Hallett and Dewitt 2007) or whether the membrane grows due to a combination of endo- and exo-cytosis (Charras et al. 2008). Nevertheless, our models clearly confirm the need for a source of membrane growth.

Equally, we should question predictions from the geometric model. Although the geometric model corresponds very well with the shell system simulations over certain regions of parameter space, there are potential phenomena that require the inclusion of certain physical effects, such as azimuthal and axial line tensions and bending moments. In particular,

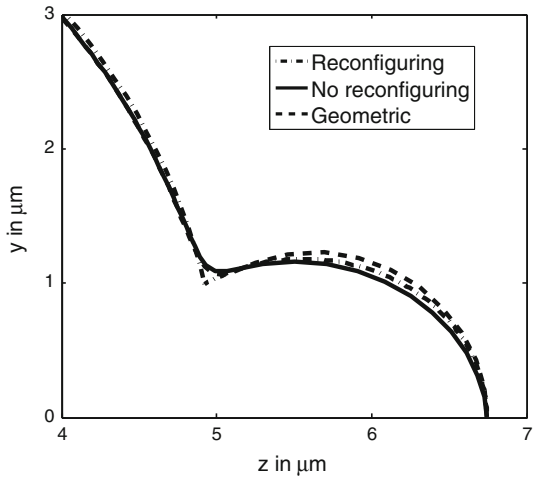

Fig. 15 Comparison between the geometric, reconfiguring and non-reconfiguring simulations. All three give qualitatively similar blebs. Parameters were chosen such that the maximum extension in each case was the same. For the geometric solution, the initial radius is $R = 5\,\mu$m and the volume fraction is $x = 0.0112$. For the non-reconfiguring solution, $A_- = 0.34\,$pN/μm, and for the reconfiguring solution, $A_- = 367.9\,$pN/μm. The update timescale was $\eta\Delta t = 0.3$. All other parameters were the same $A_+ = 10^3\,$pN/μm, $\hat{\sigma} = 1$, $\mu = 0.5$, $M = 10^{-2}\,$pNμm and the initial pressure difference was $\Delta P = 10\,$Pa

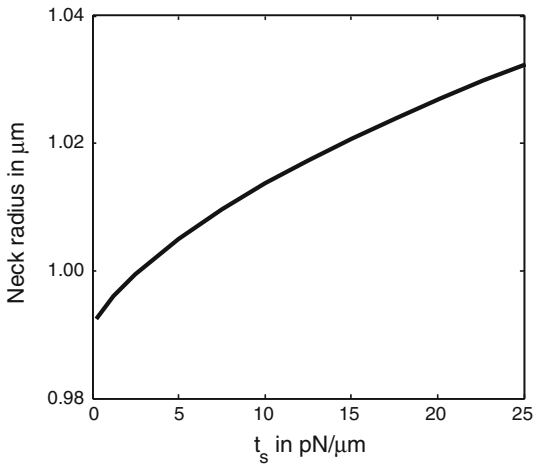

Fig. 16 Neck radius weakly increases as surface tension increases. The neck radius is the y-coordinate of the cell-body–cell-bleb transition region, i.e., $y(\sigma = \hat{\sigma})$. See "Appendix" for more details. Parameters are $A_+ = 10^3\,$pN/μm, $\mu = 0.5$, $M = 10^{-2}\,$pNμm and $\hat{\sigma} = 1$

the differences observed in Fig. 8a due to changing μ highlight the importance of considering these effects, which are often neglected when Laplace's law is simply invoked to calculate pressure differences (Tinevez et al. 2009; Charras et al. 2008). In particular, Laplace's law is invoked in (Dai and Sheetz 1999), and the linear law is shown to give a favourable match between surface tension and radius. However, their data can be interpreted as behaving non-linearly, with a positive second derivative. This relationship is observed with the generalised Laplace's law derived in Eq. (28) (data not shown).

However, by comparing results from Sects. 3, 5 and Fig. 15, we see that both geometric and non-reconfiguration systems are very similar to the more physically accurate reconfiguring system over large regions of realistic parameter values. Thus, previous models that did not consider reconfiguration still have the potential to be, at least, qualitatively correct and provide general trends that should be testable. For example, bleb volume and extension could be correlated from data allowing us to compare data against simulations and a simple geometric model.

One experimental result we are able to recover without reconfiguration is shown in Fig. 16. Here we see that, except for an initial deviation, the relationship between the neck radius and surface tension is essentially linear. This corresponds to the general trend seen in Fig. 4b of (Tinevez et al. 2009), where cells were treated with various proteins in order to generate membranes of differing surface tensions. Equally, we are able to account for the decrease in pressure difference as the bleb grows (Fig. 7a, b), which occurs as a consequence of volume conservation.

Another testable relationship is the non-monotonic response of extension with respect to increasing the amount of arc length that is weakened. Cortex ablation experiments using lasers would allow precise control over how much membrane is released (Tinevez et al. 2009). Further, depending on how bleb sizes are distributed, the narrow peak of maximal extension and quick drop off shown in Fig. 9b strongly suggest that the amount of membrane that delaminates from the cortex is tightly controlled. In the particular case where blebs are used for movement, it is imperative that the cell is able to produce blebs that are large enough to: (1) reach its substrate and (2) allow non-trivial movement once it is attached.

Even though many results can be generated with the reduced system, we have demonstrated that there are a number of quantitative responses that cannot be obtained in the absence of reconfiguration. Firstly, as the bleb grows, the pressure difference drops much quicker in the non-reconfiguring compared to the reconfiguring one. This suggests that a reconfiguring cell can produce much larger blebs than one that simply stretches its membrane. Since extremely large blebs are not naturally seen (although they can be stimulated in certain cases), it seems that the pressure difference is not the limiting factor of bleb expansion. Therefore, the expansion must be halted by another process. A potential candidate could be the rate and amount of excess membrane that the cell can produce or acquire.

Secondly, although the simulations are iterated through adiabatic steps, if we assume that reconfiguring occurs on a slower timescale than relaxation to the equilibrium state, then we are able to generate a velocity profile by using the

inherent timescale of the reconfiguration process. By comparing Fig. 14 with data not only do we reproduce the general features of a short period of very quick growth followed by a longer period of slower growth (Maugis et al. 2010), we also produce results that are of the correct quantitative size, when compared with the results of Charras et al. (2005).

This study provides a mechanical membrane model characterising blebbing as pressure-driven protrusions of an elastic shell. We have derived the model from first principles, discussing the inclusion of all pertinent assumptions and allowing us to put the purely geometric model on a more physical basis. This model is consistent with a number of experimental results. Primarily, the model generates realistically sized protrusions that correspond well to cellular blebs. Moreover, our results on the pressure difference drop during bleb initiation; velocity profiles and relationships between physical variables, such as neck radius and surface tension, have all been seen observed experimentally (Tinevez et al. 2009; Charras et al. 2005; Dai and Sheetz 1999) and underlie the importance of including membrane growth in the modelling of bleb formation.

Acknowledgments This publication is based on work supported by Award No. KUK-C1-013-04, made by King Abdullah University of Science and Technology (KAUST). AG is a Wolfson Royal Society Merit Holder and acknowledges support from a Reintegration Grant under EC Framework VII.

Appendix: Geometric model

In this appendix, we summarise the equations that relate the radius, R, of an initial sphere to the radii, r_b and r_c, of an equivalent volume system of two spheres connected through a pinned neck region, see Fig. 17. We follow the geometric construction of a blebbing cell as derived by Hu (2009).

From Fig. 17, we see that the equality

$$R\sin(\Theta) = r_c\sin(\theta_c) = r_b\sin(\theta_b), \tag{39}$$

must always hold. Further, we demand that the cell volume be constant,

$$\begin{aligned} V &= \frac{4}{3}\pi R^3 = v_c + v_b \\ &= \pi r_c^3\left(\frac{2}{3} + \cos(\theta_c) - \frac{1}{3}\cos^3(\theta_c)\right) \\ &\quad + \pi r_b^3\left(\frac{2}{3} - \cos(\theta_b) + \frac{1}{3}\cos^3(\theta_b)\right). \end{aligned} \tag{40}$$

Finally, we define the bleb volume fraction, x, as $v_b = xV$, and hence, the cell volume fraction is $v_c = (1-x)V$. This parameter x is an input to the problem.

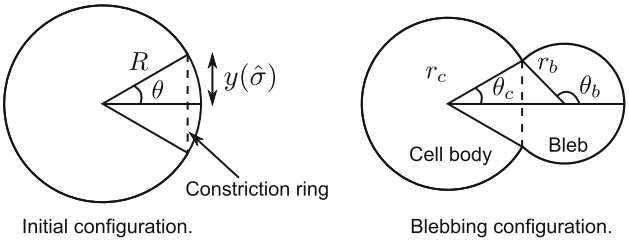

Fig. 17 Geometric model of blebbing

From Eqs. (39) and (40), we can derive equations satisfied by the radii and connection angles:

$$\begin{aligned} &16(1-x)\left(\frac{r_c}{R}\right)^3 - 3\left(\frac{r_c}{R}\right)^2\sin^4(\Theta) \\ &\quad - \left(16(1-x)^2 + \sin^6(\Theta)\right) = 0, \end{aligned} \tag{41}$$

$$\cos(\theta_c) = \frac{4(1-x) - 2\left(\frac{r_c}{R}\right)^3}{2\left(\frac{r_c}{R}\right)^3 + \left(\frac{r_c}{R}\right)\sin^2(\Theta)}, \tag{42}$$

$$\begin{aligned} &16x\left(\frac{r_b}{R}\right)^3 - 3\left(\frac{r_b}{R}\right)^2\sin^4(\Theta) \\ &\quad - \left(16x^2 + \sin^6(\Theta)\right) = 0, \end{aligned} \tag{43}$$

$$\cos(\theta_b) = \frac{-4x + 2\left(\frac{r_b}{R}\right)^3}{2\left(\frac{r_b}{R}\right)^3 + \left(\frac{r_b}{R}\right)\sin^2(\Theta)}, \tag{44}$$

where R, Θ and x all input parameters. Observe that x is varied from the initial bleb volume ratio,

$$x_0 = \frac{v_b}{V} = \frac{2 - 3\cos(\Theta) + \cos^3(\Theta)}{4}, \tag{45}$$

to the maximal bleb ratio, $1 - x_0$.

Originally, R was taken as a free variable (Hu 2009). However, using Eqs. (19)–(25) and assuming spherical symmetry of the solution, we can derive the initial radius of the unweakened cell, R. The unique solution can be seen to be:

$$y = R\sin(\theta), \tag{46}$$

$$z = R\cos(\theta), \tag{47}$$

$$s = R\theta, \tag{48}$$

$$\theta = \frac{\sigma}{\rho}, \tag{49}$$

$$t_s = \frac{\Delta PR}{2}, \tag{50}$$

$$\kappa_s = \kappa_\psi = \frac{1}{R}, \tag{51}$$

$$q_s = 0. \tag{52}$$

Substituting these back into the constitutive Eq. (16), we find

$$\frac{\Delta PR}{2} = A\left(\left(\frac{R}{\rho}\right)^2 - 1\right)(1+\mu). \tag{53}$$

The positive root of this quadratic, which depends on ΔP, ρ, A and μ, then provides the desired radius.

References

Ashby MF, Gibson LJ, Wegst U, Olive R (1995) The mechanical properties of natural materials. I. Material property charts. Proc R Soc A 450(1938):123–140

Blaser H, Reichman-Fried M, Castanon I, Dumstrei K, Marlow FL, Kawakami K, Solnica-Krezel L, Heisenberg CP, Raz E (2006) Migration of zebrafish primordial germ cells: a role for myosin contraction and cytoplasmic flow. Dev Cell 11(5):613–627

Boucrot E, Kirchhausen T (2007) Endosomal recycling controls plasma membrane area during mitosis. Proc Natl Acad Sci 104(19):7939

Charras GT (2008) A short history of blebbing. J Microsc 231(3):466–478

Charras G, Paluch E (2008) Blebs lead the way: how to migrate without lamellipodia. Nat Rev Mol Cell Biol 9(9):730–736

Charras GT, Yarrow JC, Horton MA, Mahadevan L, Mitchison TJ (2005) Non-equilibration of hydrostatic pressure in blebbing cells. Nature 435(7040):365–369

Charras GT, Coughlin M, Mitchison TJ, Mahadevan L (2008) Life and times of a cellular bleb. Biophys J 94(5):1836–1853

Collins-Hooper H, Woolley TE, Dyson L, Patel A, Potter P, Baker RE, Gaffney EA, Maini PK, Dash PR, Patel K (2012) Age-related changes in speed and mechanism of adult skeletal muscle stem cell migration. Stem Cells 30(6):1182–1195

Cunningham CC (1995) Actin polymerization and intracellular solvent flow in cell surface blebbing. J Cell Biol 129(6):1589–1599

Dai J, Sheetz MP (1999) Membrane tether formation from blebbing cells. Biophys J 77(6):3363–3370

Evans EA (1983) Bending elastic modulus of red blood cell membrane derived from buckling instability in micropipet aspiration tests. Biophys J 43(1):27–30

Evans EA, Skalak R (1980) Mechanics and thermodynamics of biomembranes. CRC Press, Boca Raton, FL

Fackler OT, Grosse R (2008) Cell motility through plasma membrane blebbing. J Cell Biol 181(6):879

Goriely A, Tabor M (2003a) Biomechanical models of hyphal growth in actinomycetes. J Theor Biol 222(2):211–218

Goriely A, Tabor M (2003b) Self-similar tip growth in filamentary organisms. Phys Rev Lett 90(10):108101

Goriely A, Tabor M (2006) Estimates of biomechanical forces in *Magnaporthe grisea*. Mycol Res 110(Pt 7):755–759

Goriely A, Károlyi G, Tabor M (2005) Growth induced curve dynamics for filamentary micro-organisms. J Math Biol 51(3):355–366

Hallett MB, Dewitt S (2007) Ironing out the wrinkles of neutrophil phagocytosis. Trends Cell Biol 17(5):209–214

Hallett MB, von Ruhland CJ, Dewitt S (2008) Chemotaxis and the cell surface-area problem. Nat Rev Mol Cell Biol 9(8):662–662

Hickson GRX, Echard A, O'Farrell PH (2006) Rho-kinase controls cell shape changes during cytokinesis. Curr Biol 16(4):359–370

Hu J (2009) Mathematical modeling and analysis of in vitro Actin filament dynamics and cell blebbing. PhD thesis, University of Minnesota

Keller H, Eggli P (1998) Protrusive activity, cytoplasmic compartmentalization, and restriction rings in locomoting blebbing Walker carcinosarcoma cells are related to detachment of cortical actin from the plasma membrane. Cell Motil Cytoskelet 41(2):181–193

Keller HU, Bebie H (1996) Protrusive activity quantitatively determines the rate and direction of cell locomotion. Cell Motil Cytoskelet 33(4):241–251

Lew DJ (2003) The morphogenesis checkpoint: how yeast cells watch their figures. Curr Opin Cell Biol 15(6):648–653

Lim FY, Chiam KH, Mahadevan L (2012) The size, shape, and dynamics of cellular blebs. Bull Am Phys Soc 55:1–6

Maugis B, Brugués J, Nassoy P, Guillen N, Sens P, Amblard F (2010) Dynamic instability of the intracellular pressure drives bleb-based motility. J Cell Sci 123(22):3884–3892

Mills JC, Stone NL, Erhardt J, Pittman RN (1998) Apoptotic membrane blebbing is regulated by myosin light chain phosphorylation. J Cell Biol 140(3):627–636

Nichol JA, Hutter OF (1996) Tensile strength and dilatational elasticity of giant sarcolemmal vesicles shed from rabbit muscle. J Phys 493:187

Norman LL, Brugs J, Sengupta K, Sens P, Aranda-Espinoza H (2010) Cell blebbing and membrane area homeostasis in spreading and retracting cells. Biophys J 99(6):1726–1733

Otto A, Collins-Hooper H, Patel A, Dash PR, Patel K (2011) Adult skeletal muscle stem cell migration is mediated by a blebbing/amoeboid mechanism. Rejuv Res 14(3):249–260

Paluch E, Sykes C, Prost J, Bornens M (2006) Dynamic modes of the cortical actomyosin gel during cell locomotion and division. Trends Cell Biol 16(1):5–10

Pozrikidis C (2001) Effect of membrane bending stiffness on the deformation of capsules in simple shear flow. J Fluid Mech 440:269–291

Pressley A (2010) Elementary differential geometry. Springer, New York

Robertson AMG, Bird CC, Waddell AW, Currie AR (1978) Morphological aspects of glucocorticoid-induced cell death in human lymphoblastoid cells. J Pathol 126(3):181–187

Russell SW, Rosenau W, Lee JC (1972) Cytolysis induced by human lymphotoxin: cinemicrographic and electron microscopic observations. Am J Pathol 69(1):103

Sahai E, Marshall CJ (2003) Differing modes of tumour cell invasion have distinct requirements for Rho/ROCK signalling and extracellular proteolysis. Nat Cell Biol 5(8):711–719

Schütz K, Keller H (1998) Protrusion, contraction and segregation of membrane components associated with passive deformation and shape recovery of Walker carcinosarcoma cells. Eur J Cell Biol 77(2):100–110

Sheetz MP, Sable JE, Döbereiner HG (2006) Continuous membrane-cytoskeleton adhesion requires continuous accommodation to lipid and cytoskeleton dynamics. Annu Rev Biophys Biomol Struct 35:417–434

Skalak R, Tozeren A, Zarda RP, Chien S (1973) Strain energy function of red blood cell membranes. Biophys J 13(3):245–264

Spangler EJ, Harvey CW, Revalee JD, Sunil Kumar PB, Laradji M (2011) Computer simulation of cytoskeleton-induced blebbing in lipid membranes. Phys Rev E 84:051906

Strychalski W, Guy RD (2012) A computational model of bleb formation. Math Med Biol 30:115–130

Tinevez JY, Schulze U, Salbreux G, Roensch J, Joanny JF, Paluch E (2009) Role of cortical tension in bleb growth. Proc Natl Acad Sci 106(44):18581–18586

Tongen A, Goriely A, Tabor M (2006) Biomechanical model for appressorial design in *Magnaporthe grisea*. J Theor Biol 240(1):1–8

Young J, Mitran S (2010) A numerical model of cellular blebbing: a volume-conserving, fluid-structure interaction model of the entire cell. J Biomech 43:210–220